Editors' Suggestion

Femtosecond trimer quench in the unconventional charge-density-wave material $1T'$-TaTe$_2$

Till Domröse and Claus Ropers[*]

Department of Ultrafast Dynamics, Max Planck Institute for Multidisciplinary Sciences, 37077 Göttingen, Germany
and 4th Physical Institute – Solids and Nanostructures, University of Göttingen, 37077 Göttingen, Germany

Ultrafast optical switching of materials properties promises future technological applications, enabled by fundamental insights about microscopic couplings and nonequilibrium phenomena. Transition-metal dichalcogenides (TMDCs) combine photosensitivity with strong correlations, furthering rich phase diagrams and enhanced tunability. The compound $1T'$-TaTe$_2$ exhibits an electronically and structurally unique set of charge density waves (CDWs), featuring an unusual increase in conductivity and amplitude modes of low prominence. Compared to other charge-ordered TMDCs, only very few studies addressed the ultrafast response of this material to optical excitation. In particular, the question whether such unconventional properties translate to unusual quench dynamics remains largely unresolved. Here, we investigate the structural dynamics in $1T'$-TaTe$_2$ by means of ultrafast nanobeam electron diffraction at an unprecedented repetition rate of 2 MHz. We reveal a strongly directional cooperative atomic motion during the one-dimensional quench of the low-temperature trimer lattice. These dynamics are completed within less than 500 fs, substantially faster than reported previously. In striking contrast, the periodic lattice distortion of the room-temperature phase is unusually robust against high-density electronic excitation. In conjunction with the known sensitivity of $1T'$-TaTe$_2$ to chemical doping, we thus expect the material to serve as a versatile platform for tunable structural control by optical stimuli.

I. INTRODUCTION

Tailoring electronic properties by chemical doping is a central element of current semiconductor technology. Transition metal dichalcogenides (TMDCs), strongly correlated materials in a chalcogen-metal-chalcogen trilayer structure [1], may lead to novel functionality [2] beyond established applications. In these compounds, comparably small modifications of the electronic state can evoke large effects via couplings to phononic, orbital or spin degrees of freedom [3,4]. Quasi-two-dimensional characteristics in conjunction with strong electron-phonon interactions promote correlated phases [5], including charge density waves (CDWs) coupled to a periodic lattice distortion (PLD) [6]. The corresponding electronic structures are highly susceptible to external stimuli [7–10] or alterations of the chemical composition [11,12] and dimensionality [13,14].

Alongside their structural tunability, TMDCs offer functionality by transient photodoping [4,15,16] and in optoelectronics [17]. Probing the interplay of structural and electronic excitations [18–60], ultrafast measurement schemes frequently uncover underlying nonequilibrium processes. In the

past, pulsed laser excitation has not only been used to drive transitions between different CDW phases [40–57], but also to induce [60] or enhance CDW order [31] as well as distinct types of disorder [32,53–56], prompt dimensional crossovers [51–53,61,62], and to drive materials into thermodynamically inaccessible metastable states [58,59,63].

To date, the investigation of ultrafast CDW dynamics and phase transitions in TMDCs has largely focused on sulfur- and selenium-based compounds [32,34–55]. In contrast, the CDW phases in TMD tellurides have only recently become the subject of ultrafast studies [64–68]. In these materials, a hybridization of the tellurium p with the metal d bands enhances the transition metal valence and thus changes the electronic texture [69,70]. Among other features, this results in an increase of the material's effective dimensionality as a result of stronger interlayer interactions [69]. Moreover, the compounds $1T'$-VTe$_2$, $1T'$-NbTe$_2$, and $1T'$-TaTe$_2$ share (3×1) superstructures with pronounced Jahn-Teller-like distortions [70], which are stable at room temperature and above [71–73].

This chemical perspective on the formation of charge-ordered superstructures in the form of tightly bound zigzag chains [69] particularly applies to $1T'$-TaTe$_2$ [73–75], the compound with the largest PLD amplitudes among the group-V compounds [73]. In this material, the trimerization even persists up to highest temperatures, i.e., an undistorted phase is absent from the phase diagram due to the electronic energy gain upon tantalum-cluster formation [69,70,76]. Cooling brings about a second transition into a unique (3×3) phase [72,76,77] that is in competition with other structural instabilities at surfaces and in few-layer systems [78–81]. Remarkably,

---

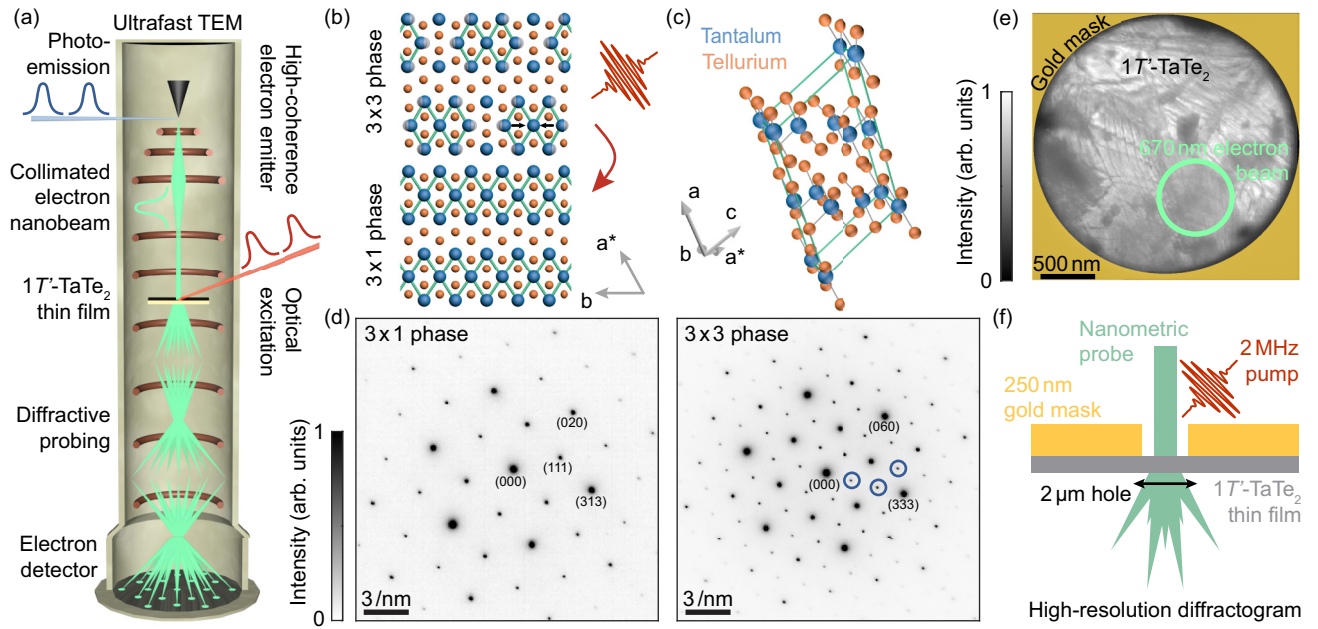[*]Contact author: claus.ropers@mpinat.mpg.de

FIG. 1. Nanobeam electron diffraction at megahertz rates in an ultrafast transmission electron microscope (UTEM). (a) Schematics of the UTEM. Ultrashort electron pulses (green) are generated via linear photoemission (blue) from a tip-shaped emitter. Laser excitation (red) drives reversible dynamics in the $1T'$-TaTe$_2$ thin film. The exceptionally high transverse beam coherence allows for collimated diffractive probing with nanometric electron illumination. (b) In-plane crystal structure of the low-temperature (3×3) (top) and the room-temperature (3×1) phases of $1T'$-TaTe$_2$ (bottom). The additional unit-cell tripling along the b axis below 174 K leads to the formation of tantalum heptamers. (c) Monoclinic unit cell (green) of $1T'$-TaTe$_2$ in the (3×1) phase. Trilayers of tantalum atoms (blue) sandwiched between tellurium atoms (orange) are stacked in threefold sequence. (d) Electron diffractograms recorded in the $[\bar{1}01]$ zone axis. In the (3×3) phase, the heptamer formation brings about PLD diffraction spots (highlighted by blue circles) in between the bright host lattice reflections present in both phases. (e) Electron micrograph of the investigated sample. In the diffraction experiments, we probe a sample area of enhanced spatial homogeneity with a diameter of 670 nm (green circle). (f) Megahertz specimen design (side view). A circular gold aperture confines the laser excitation and enables efficient heat dissipation.

the formation of the (3×3) phase results in a decrease of the electrical resistivity [82], as opposed to related transitions in other TMDCs where the opening of the CDW band gap near the Fermi energy promotes the conventional insulating behavior [1,7,47].

Its unusual phase diagram and the associated macroscopic properties call for further investigations of the CDW phases in $1T'$-TaTe$_2$. In equilibrium, the origin of the low-temperature butterfly-like structure has been linked to an anisotropic phononic softening [72,73], driven by Fermi-surface nesting [83,84]. Few ultrafast experiments studied nonequilibrium dynamics in this material, finding an only weak amplitude mode [66] and a considerably slower partial PLD suppression [65] compared to dynamics in other strongly correlated materials [40–57,67,68]. However, possible microscopic origins for a slower response remain to be explored, and a complete quench of the (3×3) phase has yet to be observed. Moreover, the sensitivity of the (3×1) periodicities to photodoping both at low and at high temperatures is of considerable interest.

In this article, we address these questions by investigating the laser-induced dynamics in $1T'$-TaTe$_2$ employing nanobeam ultrafast electron diffraction (nano-UED) in an ultrafast transmission electron microscope (UTEM) [Fig. 1(a)]. We find that the structural dynamics unfolds substantially faster than previously reported. Furthermore, the timescale of the structural quench is a strong function of excitation fluence, with a transient suppression of the (3×3) lattice distortion

proceeding as fast as 200 fs. Approaching the fluence threshold, the phase transition into the (3×1) phase is completed after 500 fs, indicative of a softening of the corresponding structural mode. In contrast, we identify an atypical stability of the high-temperature (3×1) superstructure in response to an optical stimulus, revealing the coexistence of seemingly similar types of structural order with completely different origins suspended within the same host material.

II. EXPERIMENTS AND RESULTS

A. CDW phases in $1T'$-TaTe$_2$

The basic monoclinic structure of $1T'$-TaTe$_2$ results from a commensurate distortion of the $1T$ symmetry commonly found in TMDCs. This room-temperature (3×1) phase exhibits a tripling of the (hypothetical) undistorted unit cell along the lattice vector $\mathbf{a}^*$ and a threefold layer stacking sequence [Fig. 1(c)] [72,76]. Within the unit cell, the zigzag chain formation predominantly follows from atomic displacements in a direction perpendicular to the lattice vector $\mathbf{b}$ [Fig. 1(b)] with an amplitude that amounts to up to 12.4% of the average interatomic distance. Below a temperature of 174 K, a further 7.8% distortion, mainly oriented along the $\mathbf{b}$ direction, transforms the crystal into the (3×3) phase [72,76,77]. Both phases, as well as the transition between them, primarily involve reconfigurations of the tantalum

sublattice [72] and band structure, suggesting that orbital-selective mechanisms drive the PLD [85].

Accordingly, the real-space crystal consists of a superposition of a $1T$ host with trimer periodicities, and the reciprocal lattice includes features of both types of structural symmetries. Figure 1(d) displays electron diffractograms recorded in the [$\bar{1}01$] zone axis, i.e., with the electron beam incident perpendicular on the layers spanned by the vectors **b** and **a***. In these images, the brighter diffraction spots (hkl) with $k = 3n$ (where n is an integer) correspond to the undistorted spatial periodicities (hereafter referred to as main lattice spots, see also Appendix B). In contrast, the (3×3) distortions produce the weaker reflections in between, analogous to the second-order CDW spots observed in the distorted phases of related $1T$ polytypes [1]. The intensity of these satellites is a precise measure of the (3×3) PLD amplitude $A_{3 \times 3}$, the order parameter of the structural transformation. In particular, a sinusoidal atomic structure modulation brings about a quadratic intensity scaling of first-order satellite reflections with increasing $A_{3 \times 3}$ for small atomic displacements [86]. For a commensurate superstructure, higher harmonics and linear combinations of the PLD wavevectors also exhibit structure factors of a comparable magnitude. Performing dynamical diffraction simulations (Appendix C 2), we find a quadratic scaling for all accessible satellite peaks, with deviations for relative structural changes larger than 4% (see Fig. 7 below).

B. Ultrafast pencil-beam electron diffraction

In the ultrafast experiments, we excite a $1T'$-TaTe$_2$ thin-film in the low-temperature phase with ultrashort laser pulses (800 nm wavelength, 50 fs duration, between 0.7 mJ/cm^2 and 11 mJ/cm^2 incident fluence), and probe the subsequent dynamics with collimated ultrashort electron pulses (120 keV energy, 200 fs duration, 670 nm beam diameter). To this end, the Göttingen UTEM [see Fig. 1(a) and Appendix A 1] is equipped with a laser-triggered field emitter whose nanometric size results in an exceptionally high transverse beam coherence [87]. The small effective source size promotes picometer beam emittances and high reciprocal-space resolution at narrow electron beams, enabling ultrafast diffraction measurements from sample regions of enhanced spatial homogeneity [53]. Importantly, suspending the $1T'$-TaTe$_2$ thin film below a circular gold aperture [cf. Fig. 1(f)] facilitates optimized thermal dissipation between subsequent excitation events [49,53], which allows us to induce—and accordingly probe—the dynamics at a repetition rate of 2 MHz, higher than in any previous measurement of a structural phase transition. In this way, our sample design drastically enhances the sensitivity to low-intensity features and eliminates common issues in the stroboscopic investigation of thin material films [88]. In comparison, MHz excitation in spectroscopic investigations of electronic quench dynamics typically involves considerably lower fluences [89,90].

Tracking the intensities of the (3×3) satellites at variable delay Δt between the laser pump and the electron probe pulses, the optically induced structural dynamics span four orders of magnitude [Figs. 2(a) and 5 below]. Following a rapid femtosecond suppression of the PLD amplitude, we observe a partial recovery after 5 ps for low and intermediate pump fluences. For fluences above 8 mJ/cm^2, the (3×3) intensities remain suppressed, evidencing the transition into the (3×1) phase [Fig. 2(d)]. From here, the initial state is reestablished after only 3 ns, leaving sufficient time for further relaxation and heat dissipation before the arrival of the subsequent pump pulse (after 0.5 μs). Overall, we find no significant dependence of the dynamics on the excitation wavelength in the visible spectral range (cf. Fig. 8 below).

The fastest, femtosecond features of such structural dynamics frequently approach the temporal resolution of ultrafast electron diffraction experiments given by the electron pulse length. Typically, both the exact temporal overlap as well as the pulse shape and duration are inferred from reference measurements on separate samples. Here, we provide a quantitative approach to the determination of the ultrafast instrument response function, which we believe will serve as a highly valuable benchmark for future ultrafast imaging and diffraction studies. Specifically, harnessing the versatility of the UTEM, we spectroscopically determine the inelastic scattering of electrons by the pump-induced optical near-field at the sample surface [91–93] [see Fig. 2(f) and Appendix D]. This instantaneous field-driven interaction yields a precise measure of the electron pulse shape [94]. In particular, we record such reference measurements alongside every delay curve and under the same experimental conditions, showing consistent electron pulse durations of about 200 fs. Furthermore, time zero is precisely determined for all of these curves, and thus not a free parameter during the quantitative data evaluation. The corresponding instrument resolution functions can be used to exemplify how an instantaneous signal drop would be probed [grey curves in Fig. 2(b)]. Its clear temporal separation from the measured delay curves (black points) demonstrates that the laser-induced phase switch is quantitatively resolved. For completeness, the reference measurements also allow for a deconvolution of the recorded intensity curves (colored circles), which, as expected, yields only a small correction.

Relating the spot intensities to the structural order parameter (see Appendix C 2), we extract the time constants of the transformation—a critical parameter linked to the degrees of freedom involved, thereby elucidating microscopic origins of the symmetry-broken state [42,95]. Here, the PLD suppression evolves as expected for a displacive excitation of the nuclei after a sudden quench of the electronic subsystem [96]. We thus fit the diffraction intensities for a cosinusoidal evolution of the PLD amplitude, incorporating the calibration curve obtained by the dynamical diffraction simulations [Fig. 2(c)]. We obtain half-periods from about 300 fs to 600 fs at low and at high fluence, respectively (see Appendix C 3 for all fit results). The cosine function slightly underestimates the changes to the PLD amplitude in the first few hundred femtoseconds of the dynamics (see Fig. 5 below). This observation hints at either anharmonicities in the displacive potential or a contribution from an impulsive mechanism [97]. Furthermore, the deceleration of the structural remodifications towards the end of the phase transformation is not fully captured by the model. In order to also represent the PLD suppression in a fit-model-independent manner, we quantify the melting times directly in terms of the experimentally
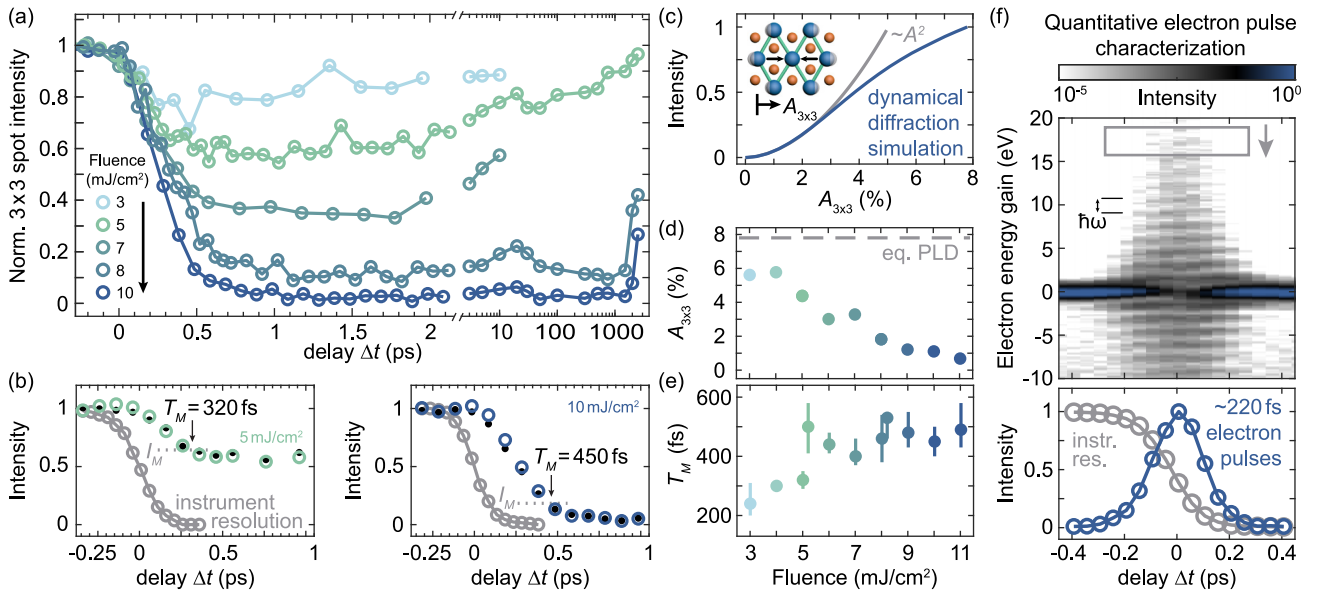
FIG. 2. Femtosecond PLD quenching in $1T'$-TaTe$_2$. (a) Delay curves derived from the intensities of second-order (3×3) diffraction spots. After a pronounced initial suppression, the PLD partially recovers for low and intermediate fluences. The material retains its initial configuration after 3 ns. (b) PLD dynamics around time zero for an excitation fluence of 5 mJ/cm^2 (left) and 10 mJ/cm^2 (right), respectively. The measured curves (black circles) display a clear temporal separation from the independently recorded instrument resolution function (grey), and the deconvoluted suppression of the (3×3) PLD (colored circles) is well resolved. (c) Dynamical diffraction simulations yield the relation between PLD amplitude $A_{3\times3}$ and spot intensities. For small atomic displacements, the intensity of second-order (3×3) spots (blue curve) increases quadratically with $A_{3\times3}$ (grey). (d) Maximum initial suppression of the PLD amplitude $A_{3\times3}$ from an equilibrium value of 7.8% for different pump fluences, based on the curve displayed in (c). A complete phase transition occurs for fluences above 8 mJ/cm^2. (e) PLD melting times T_M at different pump fluences. The phase transition slows down upon approaching the threshold excitation. (f) Laser-electron pulse cross correlation (top), obtained from the inelastic electron scattering at the optical near-field that leads to sidebands in the electron spectra separated by the photon energy $\hbar\omega$. The intensity of the outer energy sidebands yields the instrument resolution (grey, bottom) and the electron pulse shape (blue).

determined order parameter. Specifically, we evaluate the time delay for a relative suppression of 85% with respect to the minimal amplitude for each fluence. Timescales down to 200 fs are found, reaching a plateau at 460 ± 20 fs for a complete phase switch [Fig. 2(e)]. Finally, for comparison with prior studies, we also consider an exponential order parameter decay, which yields decay times between 130 fs for a weak and 430 fs for a full quench, respectively, substantially faster than a 1.4-ps exponential decay reported previously for a partial diffraction intensity suppression [65]. While it is not straightforward to reconcile such slower PLD dynamics with our results, one may consider differences in experimental parameters, including beam diameter and sample homogeneity, or different measures of time zero and pulse structure, as possible origins. Generally, propagation of excited carriers into the films may also affect the dynamics. However, in the case of a 60-nm s1T-TaS$_2$ film, thicker than the optical absorption length, above-threshold excitation was shown to rapidly switch the PLD throughout the depth [49].

The femtosecond response to an optically induced electronic transition underlines the strongly correlated nature of the (3×3) phase. Previously, a slowing-down of structural dynamics in CDW systems, similar to our observations in $1T'$-TaTe$_2$, was linked to a softening of the corresponding structural mode [98], and also identified in all-optical measurements of $1T'$-TaTe$_2$ [66]. Indeed, a comparatively flat potential landscape close to the critical point of the transition

is expected to minimize the forces driving the structural modifications, particularly for second-order and weakly first-order transitions [99].

C. Contrasting the photoresponse of the (3 × 3) and (3 × 1) orders

The temporal evolution of the second-order PLD spots evidences an ultrafast quenching of the tantalum clusters. As described in Sec. II A, however, the low-temperature phase actually results from a superposition of two stripe-like PLDs, emerging from an additional trimerization of the (3×1) order. We next investigate the photoresponse of the atomic displacements along the respective crystallographic axes individually. To this end, we probe the first-order PLD spots by changing the angle of incidence between the electron beam and the sample surface normal to approximately 0.7°. Specifically, these spots are located in the first-order Laue zone (FOLZ) and at one-third of the distance between neighboring main lattice reflections, owing to the unit-cell tripling both in and out of plane [Fig. 3(a)]. In this diffraction geometry, every main lattice spot in the FOLZ has a drastically reduced intensity, and is surrounded by three prominent satellites. Two of these are associated with the low-temperature PLD (highlighted by blue circles), and their intensity scales with the atomic displacements along the wavevector parallel to the crystal **b** axis. A third spot of the (3×1) kind (red) encodes
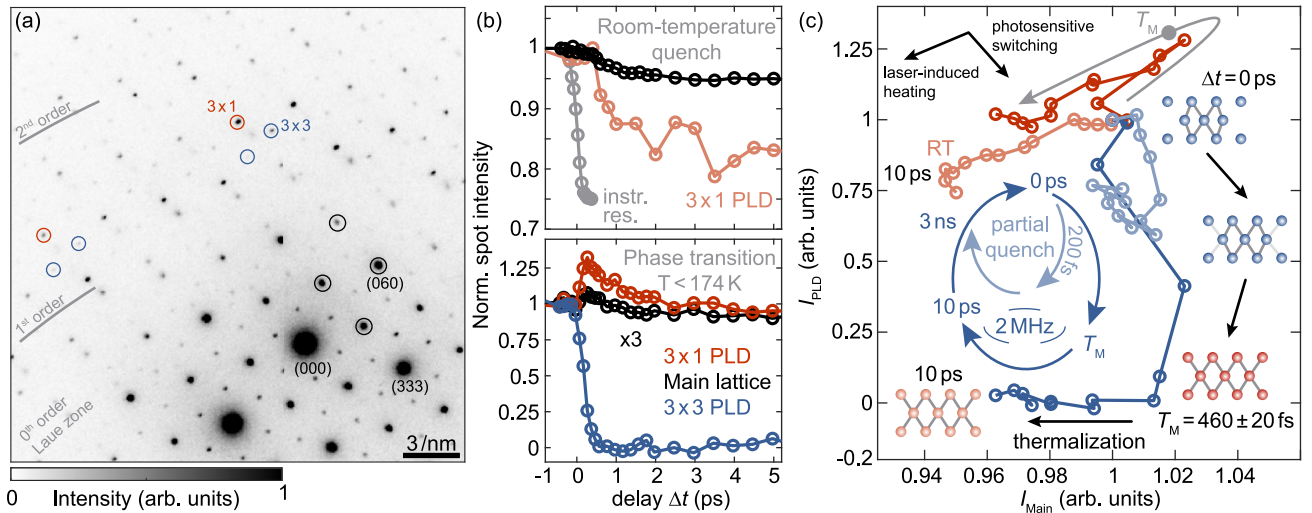
FIG. 3. Ultrafast dynamics in the first-order Laue zone and phase transition mechanism. (a) Example diffractogram for an electron beam tilted out of the $[\bar{1}01]$ zone axis. The individual signatures of the (3×1) (red circles) and the (3×3) structure (blue) reside in the first-order Laue zone, whereas the zero-order Laue zone contains second-order PLD spots and the main lattice reflections (black). (b) Temporal evolution of first-order (3×3) (blue), (3×1) (red) and of the main lattice spots (black, 10 mJ/cm^2 fluence). At room temperature (top), we observe few-picosecond Debye-Waller dynamics in all spots. During the transition from the low-temperature into the high-temperature phase (bottom), the (3×3) spots are rapidly suppressed, whereas the remaining spots display a transient overshoot before a slower, few-percent intensity decay. (c) PLD spot intensities as a function of the main lattice intensities derived from the curves displayed in (b), including temporal binning. The curves range from $\Delta t = 0 \text{ ps}$ to 10 ps. The laser-induced heating of the host lattice serves as a gauge for the photosensitivity of the two superperiodicities. The temporal evolution of the (3×1) PLD coincident to the Debye-Waller suppression indicates purely thermal dynamics both at low (dark red) and at room temperature (light red). In contrast, the (3×3) PLD can efficiently be quenched (light blue, 5 mJ/cm^2 fluence) or transformed (dark blue, 10 mJ/cm^2) optically. The corresponding intensity suppression leads to an intensity exchange with the host lattice, evolving along the vertical direction in the diagram. The laser excitation thus predominantly launches one-dimensional atomic motions towards the high-temperature (3×1) phase, followed by a few-picosecond thermalization (see also sketches of the transient crystal structures). For a partial quench, the initial trimer suppression unfolds as fast as 200 fs.

the PLD oriented perpendicular to **b**. After laser excitation, the (3×3) spots are suppressed on the same timescale as the second-order peaks, followed by a few-picosecond recovery for intermediate pump fluences [cf. Figs. 3(b) and 7 below]. As the (3×3) order disappears, diffracted intensity is redistributed into the remaining (3×1) [red curve in Fig. 3(b)] and main lattice reflections (black), leading to an intensity overshoot preceding a slower thermalization.

Based on these observations, we deduce that the phase transformation proceeds as illustrated in Fig. 3(c). The optical excitation induces a quench specifically of the trimerization oriented along the lattice vector **b**. The atomic displacements perpendicular to **b**, on the other hand, remain largely unaffected and persist even in the out-of-equilibrium state shortly after time zero. The distinction between a soft and a stable crystal axis becomes apparent by evaluating the PLD intensities during the dynamics as a function of those of the "photoinert" main lattice symmetries. A joint temporal evolution in Fig. 3(c) [derived from the curves in Fig. 3(b)] signifies thermal dynamics, indicative of an overall rise in lattice temperature, i.e., the Debye-Waller effect [24,35]. Variations towards the lower-right corner of the diagram, on the other hand, arise from an increase of main peak intensity caused by a photosensitive suppression of the PLD. Whereas the (3×3) PLD shows an immediate and strong response to the optical excitation, the (3×1) order exhibits merely thermal behavior. This remarkable difference has direct

consequences also for the non-equilibrium pathway between both phases. Specifically, we observe no sign of transient disorder during the phase transformation (cf. Figs. 6 and 9 below). As a result, the phase switching unfolds completely reversibly, resulting in unidirectional atomic motions connecting the two superstructures.

III. DISCUSSION

The large Jahn-Teller-like distortions of up to 12.4% at room temperature, and the additional PLD of 7.8% in the low-temperature phase of $1T'$-TaTe$_2$ usually suggest a description beyond that of other CDW phases [73,75]. However, the ultrafast behavior of the (3×3) distortion is indeed remarkably similar to those in related TMDCs. In that sense, the (3×3) phase parallels the (3×1) PLD in $1T'$-VTe$_2$ in terms of distortion amplitude, temperature dependence, and photosensitivity [67,68,71].

In contrast, the characteristics of the (3×1) phase appears to have no analog in other TMDCs. From a purely thermal standpoint, its stability might seem trivial due to the absence of both the $1T$ polytype and a corresponding transition temperature from the phase diagram. Optical excitation, however, has been shown to realize also thermally inaccessible metastable states [58–60,63,100] and dimensional crossovers [51–53,61,62] in a variety of related compounds. It is a particular strength of UED to map out instabilities and anisotropies

in the free-energy landscape [101] that underlie the tunability of quantum materials. For the case of $1T'$-TaTe$_2$, recent theoretical studies indeed predicts a competition between a number of structural distortions [80,81,102], experimentally realized in monolayers and at surfaces [78–80].

In our investigations of a bulk crystal, we find no sign of metastability (cf. Fig. 6 below). Similarly, after a direct excitation of the (3×1) phase of the material at room temperature, we again solely observe a thermalisation of the entire lattice also for comparably high fluences of 10 mJ/cm^2 [Figs. 3(b) and 3(c)]. In other words, also a sudden increase of the electronic temperature to several thousand Kelvin as typically achieved by pulsed laser excitation [103] is insufficient to induce femtosecond PLD dynamics. Our results underline that the formation of the two superstructures supported by the material involves completely different energy scales and driving forces, i.e., a perturbational and thus highly tunable distortion interwoven with a photoinert trimerization.

This unconventional stability among the CDW phases in TMDCs opens up interesting perspectives on exploring the origins of CDW formation in a broader sense. Recent density-functional theory calculations attribute a significant portion of the energy gain upon tantalum chain formation in bulk $1T'$-TaTe$_2$ to the stacking of the (3×1) phase [76], in agreement with the notion that the interlayer binding is enhanced in the TMD tellurides [69,70]. This implies that a more orbital-selective excitation might be required to realize transient metastable order in the material [65,85], specifically lifting the tellurium-tantalum charge transfer and thus weakening the interlayer coupling by photodoping.

Simultaneously, tuning of the material's dimensionality, can also be achieved via chemical doping [104]. Upon partially substituting the tellurium atoms with selenium in $1T$-TaSe$_{2-x}$Te$_x$, both the (3×3) and the (3×1) phase occur for doping levels down to $x > 1.3$, followed by closely related but incommensurate distortions for lower tellurium contents [105]. Interestingly, these incommensurate PLD's were found thermally stable across a broad temperature range [105,106], extending up to the complete dissociation of the host lattice [107]. Nevertheless, a subpicosecond CDW quench after 1.55 eV optical excitation was observed in $1T$-TaSeTe, implying that thermal PLD stability and a reduced photosensitivity may emerge independently in these systems [107]. In the future, spectroscopic investigations in thermal equilibrium, ultrafast methodology, and theoretical study might therefore jointly explore, among other things, the influence of electron-phonon coupling and dimensionality on CDW formation, and characterize the nonequilibrium photoresponse as a function of chemical doping in tellurides.

IV. CONCLUSIONS

In conclusion, ultrafast pencil-beam electron diffraction enables a precise mapping of the laser-induced dynamics in $1T'$-TaTe$_2$ free from the influence of structural heterogeneity. Our results suggest a close correspondence between the driving mechanisms responsible for the CDW formation at low temperatures to other related correlated phases. At the same time, the characteristics of the high-temperature phase further exemplifies behavior that is notably distinct from others in the TMDC family, warranting further investigations in the ultrafast time domain by, e.g., selectively exciting specific electronic transitions. Furthermore, the peculiar phase diagram renders $1T'$-TaTe$_2$ a promising component in heterostructures combining different layered materials [108,109]. The combination of megahertz driving and minimization of the electron beam diameter at high reciprocal-space and temporal resolution will extend the experimental possibilities to investigate nonequilibrium dynamics in such systems by means of ultrafast diffraction and imaging [30,110]. Finally, we anticipate that the precise determination of the electron pulse shape in conjunction with the high temporal resolution of nano-UED will advance the quantitative characterization of ultrafast structural dynamics and the underlying fundamental processes for a wide range of materials and heterostructures.

APPENDIX A: EXPERIMENTAL DETAILS

1. Ultrafast Transmission Electron Microscopy

The Göttingen UTEM is based on a JEOL JEM-2100F, equipped with a ZrO/W Schottky emitter [87]. Access to the ultrafast time domain is enabled by operating the electron source below the threshold for continuous electron emission, gating the linear photoemission of femtosecond electron pulses with pulsed laser illumination incident on the emitter tip (Light Conversion CARBIDE, 40 fs pulse duration, 515 nm wavelength after frequency doubling, 2 MHz repetition rate). For the optical excitation of the sample, a part of the laser output is fed into an optical parametric amplifier (Light Conversion ORPHEUS F), and converted to a wavelength between 690 nm and 940 nm. The measurements at low temperatures are conducted with a commercially available TEM sample holder that allows cooling below the phase transition temperature (Gatan Liquid Nitrogen Cooling Holder, model 636). We estimate a base temperature of 120 K in the absence of laser illumination.

In the ultrafast experiments, the data is recorded by varying the relative timing between the laser pump and the electron probe pulses in the sample plane, integrating over the average response of the sample to the optical stimulus for 90 s at every temporal delay following the stroboscopic principle. The resulting diffractograms and real-space images of the specimen were recorded with a direct electron detector (Direct Electron DE-16), and processed by an electron counting algorithm, while the static diffractograms in Fig. 1 were taken with a CCD camera (Gatan Orius). For the pulse length measurements, we used a hybrid pixel detector based on the Timepix3

chip (Amsterdam Scientific Instrument's Cheeta T3), attached behind an electron spectrometer and energy filtering device (CEOS CEFID). The size of the pump beam in the sample plane amounts to approximately $25\,\mu m$ (full-width at half-maximum), incident under an angle of around $6°$ with respect to the sample surface normal. The specified laser fluences correspond to values incident onto the samples. For the single-hole sample geometry, the local fluence may be reduced due to scattering [49]. Throughout the experiments, we observe no impact of the optical excitation on the structural integrity of the sample.

2. Sample preparation

$1T'$-TaTe$_2$ thin films with a nominal thickness of $50\,nm$ were prepared by ultramicrotomy from a commercially available single crystal (HQ graphene). The single-hole sample is produced by covering the backside of a silicon nitride membrane with an opaque gold film (thickness $250\,nm$) via argon-plasma sputtering. Electron-transparency within a $2\text{-}\mu m$ field-of-view is ensured by placing the $1T'$-TaTe$_2$ thin-film over a hole drilled by focused ion beam milling.

APPENDIX B: INDEXING OF DIFFRACTION PATTERNS

As described in the main text, the periodic lattice distortions in $1T'$-TaTe$_2$ are commensurate with the underlying, hypothetical $1T$ structure. As such, it is possible to include the three-dimensional PLD of all phases in a monoclinic unit cell. In our experiments, we record diffractograms under perpendicular incidence with respect to the individual material layers. In these images, the brightest reflections in a close to hexagonal arrangement are a signature of the reminiscent $1T$ polytype when illuminated in the corresponding [001] zone axis. For the choice of a monoclinic unit cell, this setting is analogous to the [$\bar{1}$01] zone axis, and the diffractograms require a different indexing of the depicted lattice planes, while considering systematic absences associated with the space group of $1T'$-TaTe$_2$, that is, $C2/m$ (spacegroup 12, cell choice 1 in Ref. [111]). Specifically, the [$\bar{1}$01] zone axis generally only features those spots (hkl) where $h = l$, while, additionally, only reflections with $h + k = 2n$, $h = 2n$ for $(h0l)$, $k = 2n$ for $(0kl)$, $h + k = 2n$ for $(hk0)$, $k = 2n$ for $(0k0)$, and $h = 2n$ for $(h00)$ are symmetry allowed (where n is an integer). Figure 4 shows the resulting positions of reciprocal lattice points in the ZOLZ, as recorded in the experiments for the (3×3) phase, and the corresponding indices (hkl). Reflections with $k = 3n$ describe the undistorted $1T$ periodicities, and, in this projection of the reciprocal lattice and distinct from the $1T$ polytype, the hexagons comprised out of spots with comparable distances to the direct beam are slightly distorted. Reflections in-between correspond to the (3×3) superperiodicity, analogously to the second-order CDW spots in the CDW phases of, e.g., $1T$-TaS$_2$ and $1T$-TaSe$_2$ [1]. First-order reflections of both phases appear in the first-order Laue zone, i.e., either at larger wave vectors or upon tilting the sample. For the (3×3) unit cell, their indexing fulfills $h = l + 1$ in addition to $k = 3n$ for the (3×1) and $k = 3n \pm 1$ for the (3×3) spots.
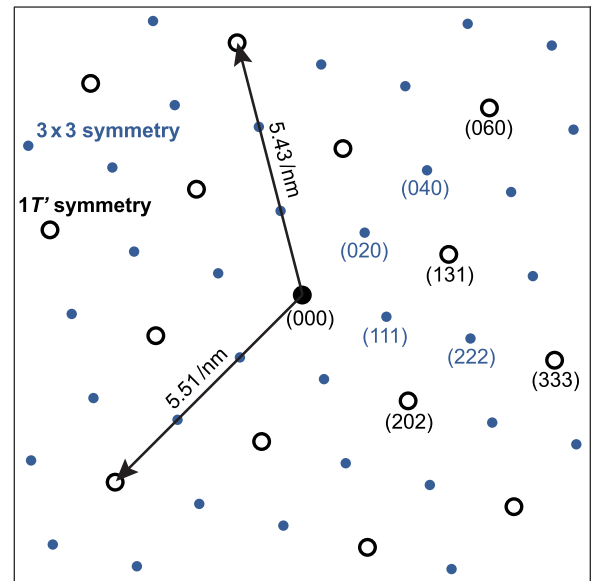

FIG. 4. Reciprocal lattice of the (3×3) phase in the projection along the [$\bar{1}$01] zone axis. The monoclinic crystal system introduces non-trivial spot-indexing of main lattice $1T'$ (black) and superstructure reflections (blue) compared to the conventional nomenclature of the $1T$ polytype. Note the different distances of second-order main lattice spots from the origin indicated by the black arrows.

APPENDIX C: DATA EVALUATION AND PHASE SWITCHING TIMES

1. Derivation of delay curves

In order to derive the delay curves displayed in Figs. 2 and 3 from the diffractogram time-series, we evaluate the intensities of first- and second-order PLD spots as well as the main lattice reflections at every temporal delay. In the following, we describe the selection of diffraction spots that contribute to the individual curves, as well as the treatment of the inelastic background in the images.

For the second-order delay curves, we sort the corresponding diffraction spots by their intensity measured before time zero, and then consider only those with an intensity that falls within the upper 40% of the detected intensity range. Afterwards, we determine the inelastic scattering contribution to every individual spot intensity. This k-dependent background is derived by radially sectioning the reciprocal lattice into 16 rings, each covering the same radial width Δk. The average signal before time zero ($\Delta t < -1\,ps$) within the individual rings, excluding the intensities of the diffraction spots they contain, yields the phononic contribution to the intensities of the second-order PLD spots within each ring. Finally, the delay curves are derived by summing the spot intensities with the background subtracted, resulting in the delay curves displayed in Fig. 5.

First-order PLD spots of the (3×3) phase are evaluated in the same manner, yielding the delay curves in Figs. 3(b) and 7(a) below. Due to the symmetry-change associated with the structural phase transformation, the number of first-order (3×1) spots is substantially reduced [see also Fig. 3(a)]. We therefore consider all (3×1) reflections in the FOLZ for
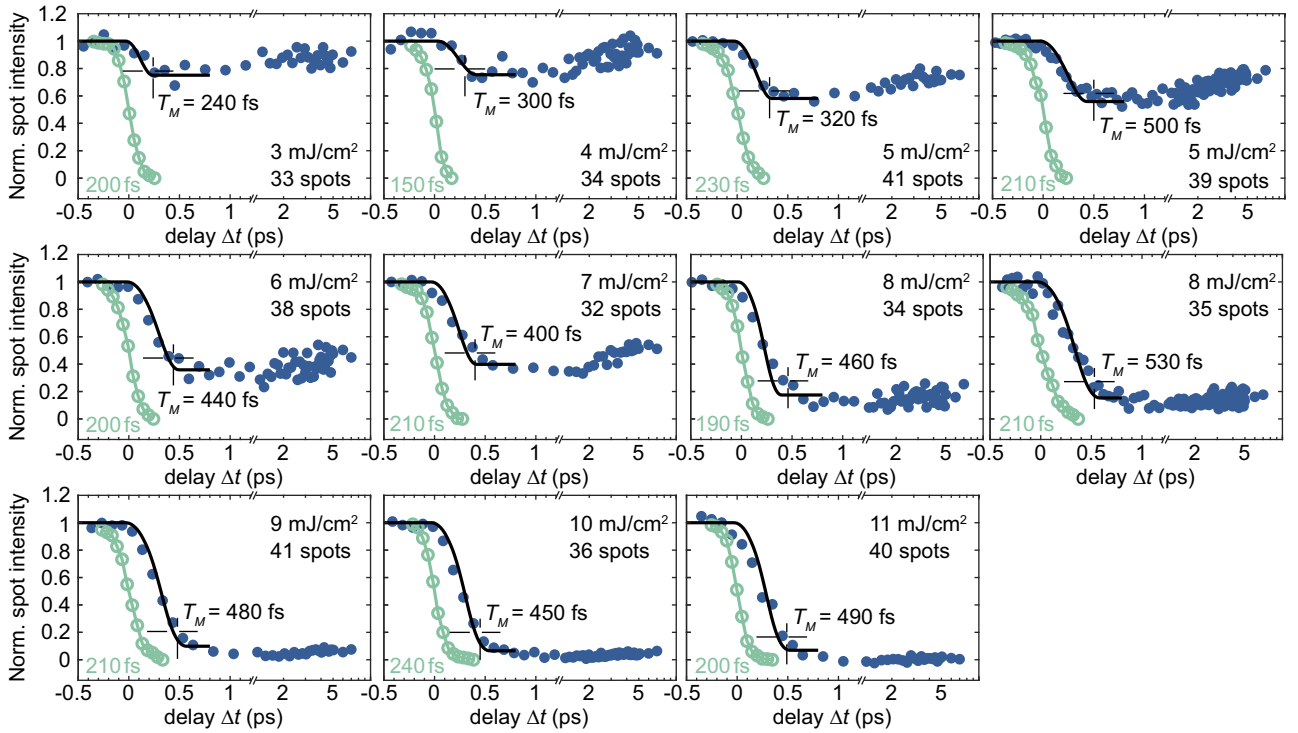
FIG. 5. Fluence-dependent delay curves of second-order CDW spots recorded in the $[\bar{1}01]$ zone axis for all incident pump fluence as discussed in Fig. 2 (blue data points), and the respective instrument response functions (green). The specified temporal resolution corresponds to the FWHM of the respective electron pulse shape. The melting time T_M is estimated from an 85% drop of the initial value with respect to the maximum suppression (black crosses). Black lines represent the cosinusoidal fit for reference.

reconstructing the temporal response of the high-temperature periodicities.

The main lattice dynamics are comprised out of all available main lattice reflections in the recorded diffractograms. As their intensity is orders of magnitude above the inelastic background, we do not subtract a phononic contribution from the recorded signal. In order to further illustrate the dynamics observed in our experiments, we additionally show representative difference images from a measurement series recorded under tilted electron illumination (Fig. 6). The images are obtained by subtracting a reference image, temporally averaged over delays smaller than -0.1 ps, from the recorded temporal evolution of the diffractograms. In agreement with the averaged delay curves, we observe a pronounced suppression of all second-order PLD spots in the ZOLZ as well as the first-order (3×3) spots in the FOLZ [blue contrast in Figs. 6(b)–6(h)]. Analogously, both the main lattice peaks and the first-order (3×1) reflections witness the transient overshoot (red contrast). Furthermore, changes of the diffracted intensities of all reflections setting in after 10 ps indicate a global oscillation of the thin film spanned across the gold aperture that also affects the diffuse background due to dynamical diffraction from neighboring intense main lattice spots.

2. Relation between spot intensities and PLD amplitude

The intensity of the (3×3) diffraction spots is a precise measure of the order parameter for the (3×3) to (3×1) transition, as it is intrinsically linked to the PLD amplitude [86]. In

order to derive a quantitative relation [Fig. 7(c)], we perform dynamical diffraction simulations [112] based on the structural refinement described in Ref. [72]. In the simulations (see Ref. [53] for a more detailed description), we average over an equal distribution in both sample thickness (in the range 40–60 nm) and sample orientation (0.2° total width around the specified zone axis). The PLD amplitude is varied by starting from the (3×3) phase, displacing the atoms in the unit cell by a global factor between 0 and 1, and along trajectories that connect their low-temperature and their high-temperature equilibrium positions. We find the same quadratic increase of the scattered intensities for first- and second-order spots with the PLD amplitudes for small distortions [86]. For larger atomic displacements, the intensities of different spot orders scale slightly differently [see dashed-black curve in Fig. 7(b)]. Based on these calibration curves, we assign a momentary PLD amplitude $A_{3\times3}(\Delta t)$ to the recorded intensities, which we then use for extracting the PLD melting time.

Tilting the electron beam out of the $[\bar{1}01]$ zone axis allows for an experimental comparison of the different types of PLD spots, accessing the ZOLZ and the FOLZ in the same image [Fig. 3(a)]. The results are displayed in Fig. 7(a), and we recover the behavior described in the main text. Importantly, both types of (3×3) reflections evolve uniformly [see also Fig. 6(i)], with small deviations for larger PLD amplitudes, i.e., in the early stages of the dynamics when the spot intensities are higher [blue curves in Fig. 7(b)]. These results are in excellent agreement with the behavior extracted from the dynamical diffraction simulations [black-dashed line; and
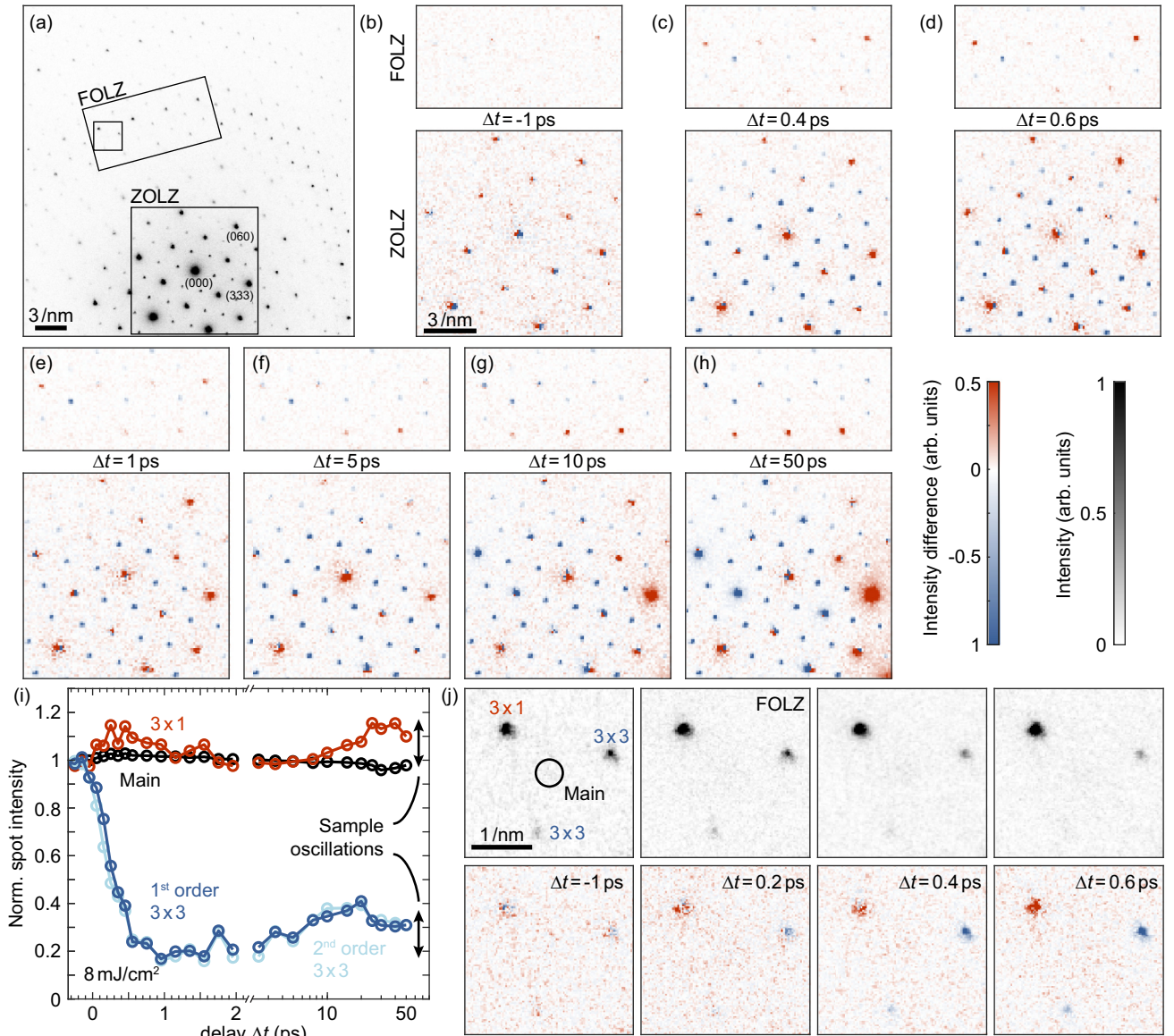
FIG. 6. Temporal evolution of diffractograms for a pump fluence of $8\,\mathrm{mJ/cm^2}$. (a) Diffractogram of $1T''$-TaTe$_2$ in the (3×3) phase, recorded under tilted electron illumination. [(b)–(h)] Difference images during the dynamics with respect to a temporally averaged diffractogram recorded before time zero. (3×3) spots appear blue and (3×1) spots are red, respectively. The top row displays dynamics in the FOLZ, whereas the bottom row shows dynamics in the ZOLZ, both highlighted in (a) by the larger black rectangles. (i) Delay curves for the different types of spots as extracted from the image series (see also Fig. 7). At delays beyond $10\,\mathrm{ps}$, an oscillation of the entire thin-film [see also the difference image in (h)] additionally modulates the intensity of all diffraction spots. (j) Example diffractograms (top) and difference images (bottom) in the FOLZ during the dynamics, derived from the region highlighted by the black square in (a). The optical excitation induces intensity variations, while no sign of transient disorder in the form of spot broadening is visible for neither type of first-order spot.

Fig. 7(c)], underlining the highly quantitative characterization of the phase transformation in our measurements.

3. Fitting the PLD amplitude suppression

As described in the main text, we evaluate the PLD melting time by different fit functions. All of these approaches are calibrated by the relation between the recorded intensities and the PLD amplitude derived from dynamical diffraction simulations as described in Appendix C 2.

For a displacive excitation mechanism [96], we fit the intensities of the second-order spots to a cosinusoidal suppression of the PLD amplitude $A(t)$ with

$$A(t) = \begin{cases} A_0, & t \leqslant 0 \\ \Delta A \cos\left(\frac{\pi t}{T_{\mathrm{M}}}\right) + \frac{A_0 + A_{\min}}{2}, & 0 < t < T_{\mathrm{M}}. \end{cases} \quad \text{(C1)}$$

Therein, $\Delta A = \frac{A_0 - A_{\min}}{2}$, with the initial PLD amplitude before time zero A_0 and the minimum value after the structural quench $A_{\min}$. T_{M} is the melting time, corresponding to a half-cycle of the cosinusoidal PLD suppression. Importantly, and as detailed in the main text, time zero is a measured quantity and thus not a fit parameter. In a second approach, we consider
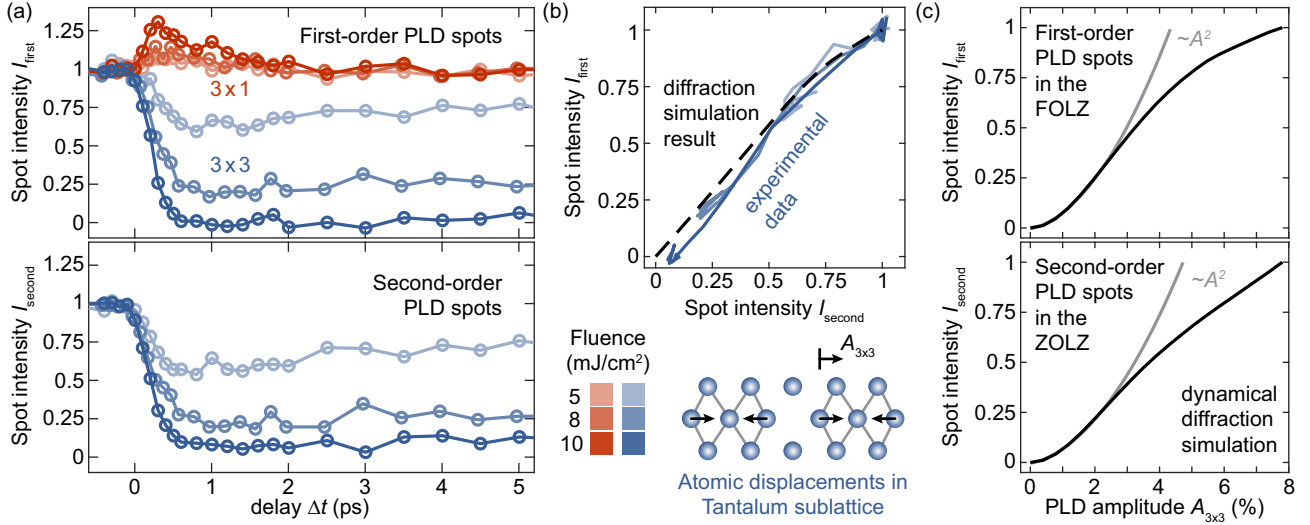
FIG. 7. Fluence-dependent delay curves and comparison of PLD spots of different order under tilted electron illumination (cf. Fig. 6). (a) Temporal evolution of intensities scattered into first-order (top) and second-order diffraction spots (bottom) of the (3×1) (red) and the (3×3) (blue) type for different excitation fluences. The high-temperature PLD spots display a transient overshoot that scales with the pump fluence, followed by a slower thermalization (see main text). (3×3) spots of both first and second order are suppressed within 500 fs. (b) PLD spot intensities of second-order spots as a function of first-order (3×3) intensities as displayed in (a). Both types of spots encode the same scaling with the PLD amplitude such that their laser-induced suppression during the structural transformation into the (3×1) phase is almost identical. The measured relationship follows the expected behavior derived from dynamical diffraction simulations (dashed-black line). (c) Simulated dependence of PLD spot intensities on the PLD amplitude for first-order (top) and second-order (3×3) spots (bottom). For structural distortions smaller than 4% of the respective average interatomic distances (see also sketch), dynamical diffraction simulations recover the expected quadratic scaling (grey), with deviations for larger atomic displacements.

an exponential decay of the order parameter, where

$$
A(t) = \begin{cases} A_0, & t \leqslant 0 \\ (A_0 - A_{\min})\, e^{-t/\tau} + A_{\min}, & t > 0. \end{cases} \quad \text{(C2)}
$$

The extracted time constant τ corresponds to a relative PLD amplitude suppression of 63%. The fit results for the individual pump fluences are listed in Table I, along with the

TABLE I. Experimentally derived melting times based on the different methods and fit functions described in the text.

Fluence [mJ/cm^2]	85% suppression T_M[fs]	Exponential decay τ[fs]	Displacive excitation T_M[fs]
3	240^{+70}_{-40}	130 ± 60	260 ± 100
4	300^{+20}_{-10}	290 ± 180	380 ± 90
5	320^{+30}_{-30}	160 ± 40	370 ± 30
5	500^{+80}_{-90}	300 ± 60	460 ± 30
6	440^{+40}_{-30}	260 ± 70	510 ± 110
7	400^{+60}_{-30}	240 ± 70	440 ± 40
8	460^{+80}_{-80}	270 ± 50	420 ± 40
8	530^{+20}_{-70}	360 ± 40	610 ± 30
9	480^{+70}_{-50}	430 ± 60	600 ± 20
10	450^{+50}_{-50}	320 ± 40	580 ± 20
11	490^{+90}_{-60}	430 ± 120	550 ± 50

results from inferring the transition time directly from the experimental data, i.e., without assuming a specific function underlying the observed dynamics. To this end, we extract the temporal delay where the recorded PLD spot intensity first falls below a value that corresponds to 85% of the overall intensity drop at the respective fluence. In order to also quantify the measurement uncertainties of this determination, we estimate the noise level in terms of the relative intensity variations ΔI recorded before time zero. For datasets with a particularly low noise level, we instead define a minimum ΔI of 5%. The error bars displayed in Figs. 2(e) and 8(b) are derived by finding the temporal delay where the described relative intensity suppression amounts to $(85 \pm \Delta I)\%$.

4. Wavelength-dependent measurements

We additionally explore the dependence of the CDW dynamics in $1T'$-TaTe$_2$ in the visible spectral range by recording delay curves at laser wavelengths between 690 nm and 940 nm. The results are depicted in Fig. 8. In the considered wavelength regime, we expect comparable laser absorption profiles given the close-to constant optical conductivity and reflectivity of the material [66]. We find similar melting times in all of these measurements, in line with the results from the fluence-dependent characterization for an 800 nm-excitation described in the main text. Due to pump-laser instabilities, the noise level in the measurements for 750 nm- and 880 nm-excitation is slightly enhanced.
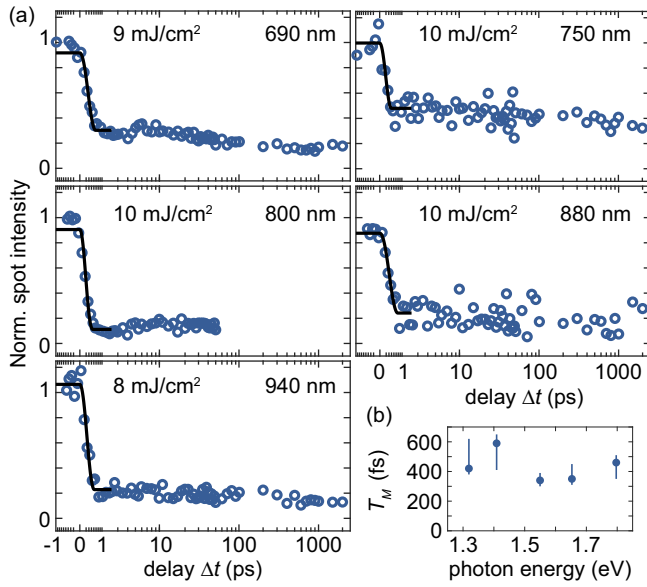
FIG. 8. CDW dynamics at different excitation wavelengths in the visible spectrum. (a) Irrespective of the incident pump photon energy, the second-order spots of the (3×3) phase (blue circles) are suppressed within 500 fs. The black curves represent the results of the cosinusoidal fits. (b) PLD melting time derived from the 85% intensity suppression as described in the text. We observe no significant influence of the pump photon energy on the temporal evolution of the dynamics.

APPENDIX D: ELECTRON PULSE DURATION AND INSTRUMENT RESOLUTION FUNCTION

The electron pulse duration is obtained by measuring the instantaneous inelastic interaction of the electron pulses with the optical near-field at the surface of the specimen (photon-induced near-field electron microscopy, PINEM [91–94,113]). Therein, individual electrons either gain or lose energy in multiple integers of the photon energy, leading to characteristic sidebands in the electron spectra when they are in spatiotemporal overlap with the laser illumination. The number of electrons that interact with the light field and the extent of the energy exchange, i.e., the population and the overall number of energy sidebands, respectively, strongly depends on the optical field strength. A typical cross correlation of electron and laser pulses obtained by scanning the temporal delay between both pulses is depicted in Fig. 2(f). In particular, the occupation of the outermost sideband possesses a linear field-dependence [92]. Summing up the scattered intensity in this energy regime thus yields a precise measure of the electron pulse structure, effectively removing the laser pulse duration from the cross correlation [94]. The resulting instrument resolution functions [Figs. 2(b) and 5] describe how the experimental setup would resolve an abrupt, step-like structural change.

APPENDIX E: TEMPORAL EVOLUTION OF THE DIFFRACTION SPOT SHAPE

In the recorded diffractograms, the long-range coherence of the CDW is encoded in the temporal evolution of the shape
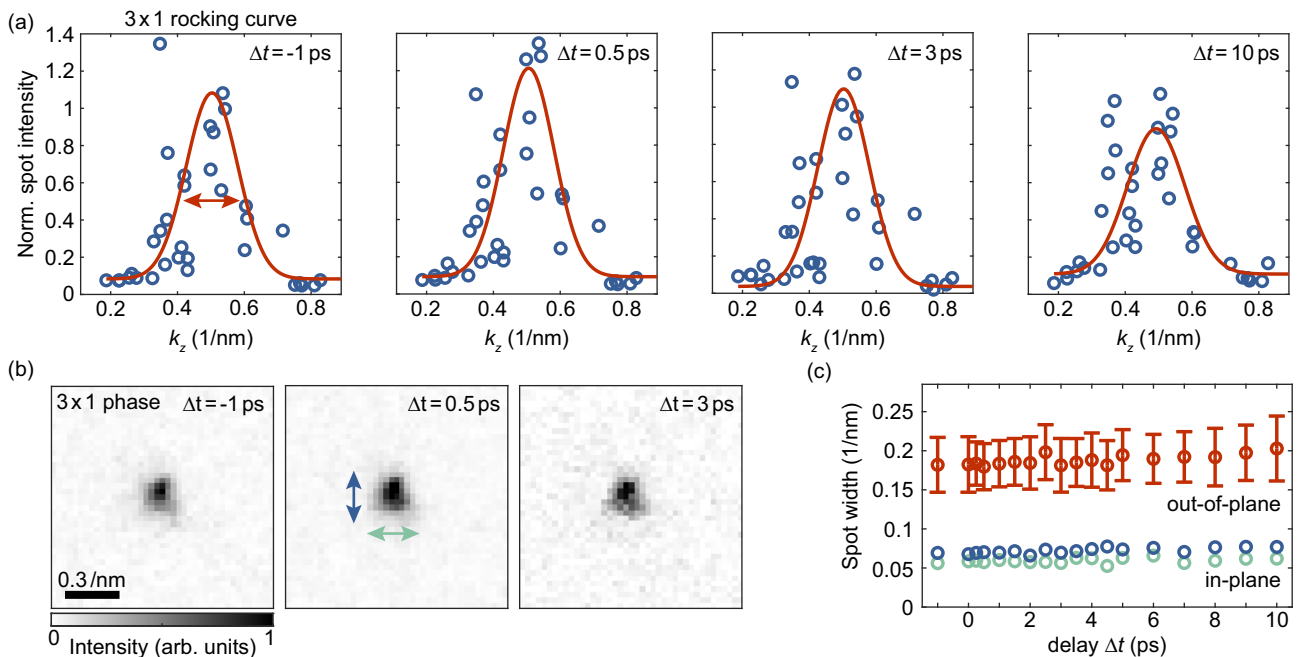

FIG. 9. Three-dimensional temporal evolution of the (3×1) diffraction spot shape. (a) (3×1) rocking curves as extracted from a single measurement under tilted illumination for an excitation fluence of $8\,\text{mJ/cm}^2$. At every temporal delay, every data point (blue circles) corresponds to the intensity of one individual (3×1) diffraction spot situated at out-of-plane momentum k_z. The resulting rocking curve (red), centered around a value for k_z that corresponds to the threefold stacking, preserves its width during the dynamics. (b) In-plane spot profile of a representative individual (3×1) reflection. Similar to (a), the spot shape does not change during the phase transformation. (c) Diffraction spot widths (FWHM) resulting from a fit of a gaussian spot shape to the data displayed in (a) and (b). The error bars represent the 68% confidence interval of the fit results for the respective in-plane (green and blue) and the out-of-plane values (red).

of the individual CDW diffraction spots. As such, disorder along the in-plane direction would result in a broadening of the corresponding (3×1) or the (3×3) reflections. In our experiments, such a broadening is absent regardless of the laser pump fluence, indicating that the phase transformation does not involve the transient generation of topological defects [cf. Figs. 6, 9(b), and 9(c)]. Similarly, the out-of-plane coherence, i.e., the CDW stacking sequence, can be inferred from a reconstruction of the CDW rocking curve [Fig. 9(a)]. To this end, electron diffractograms recorded under tilted-beam conditions feature multiple Laue zones [cf. Fig. 3(a)] that allow to densely sample the CDW diffraction spot shape at different out-of-plane momenta [53]. We assume that the most intense (3×1) spots in our images are situated in the first-order Laue zone at an out-of-plane momentum corresponding to the threefold CDW stacking sequence. The

resulting rocking curves are shown in Fig. 9(a). Generally, the occurrence of possible disorder along the layer direction is more difficult to resolve than comparable in-plane processes due to the strong influence of dynamical scattering on diffracted intensities. Nevertheless, a dimensional crossover during the dynamics would result in a pronounced intensity increase that is distributed homogeneously along the out-of-plane momentum k_z [53]. As such a dynamics is absent in our data, we conclude that the optical excitation does not induce transient disorder during the dynamics. Instead, the observed intensity overshoot and the subsequent (3×1) suppression described in the main text maintains the three-dimensional shape of the diffraction spots throughout the entire dynamics. Similarly, the first-order (3×3) spots show no sign of transient spot broadening, as evident from the difference images displayed in Fig. 6.

[1] J. A. Wilson, F. J. Di Salvo, and S. Mahajan, Charge-density waves and superlattices in the metallic layered transition metal dichalcogenides, Adv. Phys. **24**, 117 (1975).

[2] D. Jariwala, V. K. Sangwan, L. J. Lauhon, T. J. Marks, and M. C. Hersam, Emerging device applications for semiconducting two-dimensional transition metal dichalcogenides, ACS Nano **8**, 1102 (2014).

[3] Y. Tokura, M. Kawasaki, and N. Nagaosa, Emergent functions of quantum materials, Nat. Phys. **13**, 1056 (2017).

[4] D. N. Basov, R. D. Averitt, and D. Hsieh, Towards properties on demand in quantum materials, Nat. Mater. **16**, 1077 (2017).

[5] W. Li, X. Qian, and J. Li, Phase transitions in 2D materials, Nat. Rev. Mater. **6**, 829 (2021).

[6] K. Rossnagel, On the origin of charge-density waves in select layered transition-metal dichalcogenides, J. Phys.: Condens. Matter **23**, 213001 (2011).

[7] M. Yoshida, R. Suzuki, Y. Zhang, M. Nakano, and Y. Iwasa, Memristive phase switching in two-dimensional $1T$-TaS_2 crystals, Sci. Adv. **1**, e1500606 (2015).

[8] M. M. Ugeda, A. J. Bradley, Y. Zhang, S. Onishi, Y. Chen, W. Ruan, C. Ojeda-Aristizabal, H. Ryu, M. T. Edmonds, H.-Z. Tsai *et al.*, Characterization of collective ground states in single-layer $NbSe_2$, Nat. Phys. **12**, 92 (2016).

[9] D. Schmitt, J. P. Bange, W. Bennecke, A. AlMutairi, G. Meneghini, K. Watanabe, T. Taniguchi, D. Steil, D. R. Luke, R. T. Weitz *et al.*, Formation of moiré interlayer excitons in space and time, Nature (London) **608**, 499 (2022).

[10] G. Jarc, S. Y. Mathengattil, A. Montanaro, F. Giusti, E. M. Rigoni, R. Sergo, F. Fassioli, S. Winnerl, S. Dal Zilio, D. Mihailovic *et al.*, Cavity-mediated thermal control of metal-to-insulator transition in $1T$-TaS_2, Nature (London) **622**, 487 (2023).

[11] R. Ang, Y. Miyata, E. Ieki, K. Nakayama, T. Sato, Y. Liu, W. J. Lu, Y. P. Sun, and T. Takahashi, Superconductivity and bandwidth-controlled Mott metal-insulator transition in $1T$-$TaS_{2-x}Se_x$, Phys. Rev. B **88**, 115145 (2013).

[12] H. Luo, W. Xie, J. Tao, I. Pletikosic, T. Valla, G. S. Sahasrabudhe, G. Osterhoudt, E. Sutton, K. S. Burch, E. M. Seibel *et al.*, Differences in chemical doping matter: Superconductivity in $Ti_{1-x}Ta_xSe_2$ but not in $Ti_{1-x}Nb_xSe_2$, Chem. Mater. **28**, 1927 (2016).

[13] F. B. Meng, Z. Liu, L. X. Yang, M. Z. Shi, B. H. Ge, H. Zhang, J. J. Ying, Z. F. Wang, Z. Y. Wang, T. Wu, and X. H. Chen, Metal-insulator transition in organic ion intercalated VSe_2 induced by dimensional crossover, Phys. Rev. B **102**, 165410 (2020).

[14] S. H. Sung, N. Schnitzer, S. Novakov, I. El Baggari, X. Luo, J. Gim, N. M. Vu, Z. Li, T. H. Brintlinger, Y. Liu *et al.*, Two-dimensional charge order stabilized in clean polytype heterostructures, Nat. Commun. **13**, 413 (2022).

[15] A. de la Torre, D. M. Kennes, M. Claassen, S. Gerber, J. W. McIver, and M. A. Sentef, *Colloquium:* Nonthermal pathways to ultrafast control in quantum materials, Rev. Mod. Phys. **93**, 041002 (2021).

[16] C. Bao, P. Tang, D. Sun, and S. Zhou, Light-induced emergent phenomena in 2D materials and topological materials, Nat. Rev. Phys. **4**, 33 (2022).

[17] K. F. Mak and J. Shan, Photonics and optoelectronics of 2D semiconductor transition metal dichalcogenides, Nat. Photon. **10**, 216 (2016).

[18] C. W. Siders, A. Cavalleri, K. Sokolowski-Tinten, Cs. Tóth, T. Guo, M. Kammler, M. H. von Hoegen, K. R. Wilson, D. von der Linde, and C. P. J. Barty, Detection of nonthermal melting by ultrafast x-ray diffraction, Science **286**, 1340 (1999).

[19] A. M. Lindenberg, I. Kang, S. L. Johnson, T. Missalla, P. A. Heimann, Z. Chang, J. Larsson, P. H. Bucksbaum, H. C. Kapteyn, H. A. Padmore, R. W. Lee, J. S. Wark, and R. W. Falcone, Time-resolved x-ray diffraction from coherent phonons during a laser-induced phase transition, Phys. Rev. Lett. **84**, 111 (2000).

[20] K. Sokolowski-Tinten, C. Blome, J. Blums, A. Cavalleri, C. Dietrich, A. Tarasevitch, I. Uschmann, E. Förster, M. Kammler, M. Horn-von-Hoegen, and D. von der Linde, Femtosecond x-ray measurement of coherent lattice vibrations near the Lindemann stability limit, Nature (London) **422**, 287 (2003).

[21] B. J. Siwick, J. R. Dwyer, R. E. Jordan, and R. J. D. Miller, An atomic-level view of melting using femtosecond electron diffraction, Science **302**, 1382 (2003).

[22] P. Beaud, A. Caviezel, S. O. Mariager, L. Rettig, G. Ingold, C. Dornes, S.-W. Huang, J. A. Johnson, M. Radovic, T. Huber

et al., A time-dependent order parameter for ultrafast photoinduced phase transitions, Nat. Mater. **13**, 923 (2014).

[23] S. Gerber, S.-L. Yang, D. Zhu, H. Soifer, J. A. Sobota, S. Rebec, J. J. Lee, T. Jia, B. Moritz, C. Jia *et al.*, Femtosecond electron-phonon lock-in by photoemission and x-ray free-electron laser, Science **357**, 71 (2017).

[24] L. Waldecker, R. Bertoni, H. Hübener, T. Brumme, T. Vasileiadis, D. Zahn, A. Rubio, and R. Ernstorfer, Momentum-resolved view of electron-phonon coupling in multilayer WSe_2, Phys. Rev. Lett. **119**, 036803 (2017).

[25] S. Wall, S. Yang, L. Vidas, M. Chollet, J. M. Glownia, M. Kozina, T. Katayama, T. Henighan, M. Jiang, T. A. Miller *et al.*, Ultrafast disordering of vanadium dimers in photoexcited VO_2, Science **362**, 572 (2018).

[26] E. J. Sie, C. M. Nyby, C. D. Pemmaraju, S. J. Park, X. Shen, J. Yang, M. C. Hoffmann, B. K. Ofori-Okai, R. Li, A. H. Reid *et al.*, An ultrafast symmetry switch in a Weyl semimetal, Nature (London) **565**, 61 (2019).

[27] S. R. Tauchert, M. Volkov, D. Ehberger, D. Kazenwadel, M. Evers, H. Lange, A. Donges, A. Book, W. Kreuzpaintner, U. Nowak, and P. Baum, Polarized phonons carry angular momentum in ultrafast demagnetization, Nature (London) **602**, 73 (2022).

[28] D. Filippetto, P. Musumeci, R. K. Li, B. J. Siwick, M. R. Otto, M. Centurion, and J. P. F. Nunes, Ultrafast electron diffraction: Visualizing dynamic states of matter, Rev. Mod. Phys. **94**, 045004 (2022).

[29] M. Buzzi, M. Först, R. Mankowsky, and A. Cavalleri, Probing dynamics in quantum materials with femtosecond x-rays, Nat. Rev. Mater. **3**, 299 (2018).

[30] F. M. Alcorn, P. K. Jain, and R. M. van der Veen, Time-resolved transmission electron microscopy for nanoscale chemical dynamics, Nat. Rev. Chem. **7**, 256 (2023).

[31] A. Singer, S. K. K. Patel, R. Kukreja, V. Uhlíř, J. Wingert, S. Festersen, D. Zhu, J. M. Glownia, H. T. Lemke, S. Nelson, M. Kozina, K. Rossnagel, M. Bauer, B. M. Murphy, O. M. Magnussen, E. E. Fullerton, and O. G. Shpyrko, Photoinduced enhancement of the charge density wave amplitude, Phys. Rev. Lett. **117**, 056401 (2016).

[32] Y. Cheng, A. Zong, L. Wu, Q. Meng, W. Xia, F. Qi, P. Zhu, X. Zou, T. Jiang, Y. Guo *et al.*, Ultrafast formation of topological defects in a two-dimensional charge density wave, Nat. Phys. **20**, 54 (2024).

[33] F. Kurtz, T. N. Dauwe, S. V. Yalunin, G. Storeck, J. G. Horstmann, H. Böckmann, and C. Ropers, Non-thermal phonon dynamics and a quenched exciton condensate probed by surface-sensitive electron diffraction, Nat. Mater. **23**, 890 (2024).

[34] G. Storeck, J. G. Horstmann, T. Diekmann, S. Vogelgesang, G. von Witte, S. V. Yalunin, K. Rossnagel, and C. Ropers, Structural dynamics of incommensurate charge-density waves tracked by ultrafast low-energy electron diffraction, Struct. Dyn. **7**, 034304 (2020).

[35] M. R. Otto, J.-H. Pöhls, L. P. René de Cotret, M. J. Stern, M. Sutton, and B. J. Siwick, Mechanisms of electron-phonon coupling unraveled in momentum and time: The case of soft phonons in $TiSe_2$, Sci. Adv. **7**, eabf2810 (2021).

[36] D. R. Cremons, D. A. Plemmons, and D. J. Flannigan, Defect-mediated phonon dynamics in TaS_2 and WSe_2, Struct. Dyn. **4**, 044019 (2017).

[37] A. Mann, E. Baldini, A. Odeh, A. Magrez, H. Berger, and F. Carbone, Probing the coupling between a doublon excitation and the charge-density wave in TaS_2 by ultrafast optical spectroscopy, Phys. Rev. B **94**, 115122 (2016).

[38] L. Perfetti, P. A. Loukakos, M. Lisowski, U. Bovensiepen, M. Wolf, H. Berger, S. Biermann, and A. Georges, Femtosecond dynamics of electronic states in the Mott insulator $1T$-TaS_2 by time resolved photoelectron spectroscopy, New J. Phys. **10**, 053019 (2008).

[39] T. Rohwer, S. Hellmann, M. Wiesenmayer, C. Sohrt, A. Stange, B. Slomski, A. Carr, Y. Liu, L. M. Avila, M. Kalläne *et al.*, Collapse of long-range charge order tracked by time-resolved photoemission at high momenta, Nature (London) **471**, 490 (2011).

[40] M. Eichberger, H. Schäfer, M. Krumova, M. Beyer, J. Demsar, H. Berger, G. Moriena, G. Sciaini, and R. J. D. Miller, Snapshots of cooperative atomic motions in the optical suppression of charge density waves, Nature (London) **468**, 799 (2010).

[41] N. Erasmus, M. Eichberger, K. Haupt, I. Boshoff, G. Kassier, R. Birmurske, H. Berger, J. Demsar, and H. Schwoerer, Ultrafast dynamics of charge density Waves in $4H_b$-$TaSe_2$ probed by femtosecond electron diffraction, Phys. Rev. Lett. **109**, 167402 (2012).

[42] C. Sohrt, A. Stange, M. Bauer, and K. Rossnagel, How fast can a Peierls-Mott insulator be melted? Faraday Discuss. **171**, 243 (2014).

[43] T.-R. T. Han, F. Zhou, C. D. Malliakas, P. M. Duxbury, S. D. Mahanti, M. G. Kanatzidis, and C.-Y. Ruan, Exploration of metastability and hidden phases in correlated electron crystals visualized by femtosecond optical doping and electron crystallography, Sci. Adv. **1**, e1400173 (2015).

[44] K. Haupt, M. Eichberger, N. Erasmus, A. Rohwer, J. Demsar, K. Rossnagel, and H. Schwoerer, Ultrafast metamorphosis of a complex charge-density wave, Phys. Rev. Lett. **116**, 016402 (2016).

[45] L. Le Guyader, T. Chase, A. H. Reid, R. K. Li, D. Svetin, X. Shen, T. Vecchione, X. J. Wang, D. Mihailovic, and H. A. Dürr, Stacking order dynamics in the quasi-two-dimensional dichalcogenide $1T$-TaS_2 probed with MeV ultrafast electron diffraction, Struct. Dyn. **4**, 044020 (2017).

[46] A. Zong, X. Shen, A. Kogar, L. Ye, C. Marks, D. Chowdhury, T. Rohwer, B. Freelon, S. Weathersby, R. Li, J. Yang, J. Checkelsky, X. Wang, and N. Gedik, Ultrafast manipulation of mirror domain walls in a charge density wave, Sci. Adv. **4**, eaau5501 (2018).

[47] K. Sun, S. Sun, C. Zhu, H. Tian, H. Yang, and J. Li, Hidden CDW states and insulator-to-metal transition after a pulsed femtosecond laser excitation in layered chalcogenide $1T$-$TaS_{2−x}Se_x$, Sci. Adv. **4**, eaas9660 (2018).

[48] S. Ji, O. Grånäs, K. Rossnagel, and J. Weissenrieder, Transient three-dimensional structural dynamics in $1T$-$TaSe_2$, Phys. Rev. B **101**, 094303 (2020).

[49] T. Danz, T. Domröse, and C. Ropers, Ultrafast nanoimaging of the order parameter in a structural phase transition, Science **371**, 371 (2021).

[50] Y. Zhang, X. Shi, M. Guan, W. You, Y. Zhong, T. R. Kafle, Y. Huang, H. Ding, M. Bauer, K. Rossnagel, S. Meng, H. C. Kapteyn, and M. M. Murnane, Creation of a novel inverted charge density wave state, Struct. Dyn. **9**, 014501 (2022).

[51] P. Chen, Y.-H. Chan, X.-Y. Fang, S.-K. Mo, Z. Hussain, A.-V. Fedorov, M. Y. Chou, and T.-C. Chiang, Hidden order and dimensional crossover of the charge density waves in TiSe$_2$, Sci. Rep. **6**, 37910 (2016).

[52] Y. Cheng, A. Zong, J. Li, W. Xia, S. Duan, W. Zhao, Y. Li, F. Qi, J. Wu, L. Zhao *et al.*, Light-induced dimension crossover dictated by excitonic correlations, Nat. Commun. **13**, 963 (2022).

[53] T. Domröse, T. Danz, S. F. Schaible, K. Rossnagel, S. V. Yalunin, and C. Ropers, Light-induced hexatic state in a layered quantum material, Nat. Mater. **22**, 1345 (2023).

[54] C. Laulhé, T. Huber, G. Lantz, A. Ferrer, S. O. Mariager, S. Grübel, J. Rittmann, J. A. Johnson, V. Esposito, A. Lübcke, L. Huber, M. Kubli, M. Savoini, V. L. R. Jacques, L. Cario, B. Corraze, E. Janod, G. Ingold, P. Beaud, S. L. Johnson *et al.*, Ultrafast formation of a charge density wave state in 1T-TaS$_2$: Observation at nanometer scales using time-resolved x-ray diffraction, Phys. Rev. Lett. **118**, 247401 (2017).

[55] S. Vogelgesang, G. Storeck, J. G. Horstmann, T. Diekmann, M. Sivis, S. Schramm, K. Rossnagel, S. Schäfer, and C. Ropers, Phase ordering of charge density waves traced by ultrafast low-energy electron diffraction, Nat. Phys. **14**, 184 (2018).

[56] A. Zong, A. Kogar, Y.-Q. Bie, T. Rohwer, C. Lee, E. Baldini, E. Ergeçen, M. B. Yilmaz, B. Freelon, E. J. Sie *et al.*, Evidence for topological defects in a photoinduced phase transition, Nat. Phys. **15**, 27 (2019).

[57] J. G. Horstmann, H. Böckmann, B. Wit, F. Kurtz, G. Storeck, and C. Ropers, Coherent control of a surface structural phase transition, Nature (London) **583**, 232 (2020).

[58] L. Stojchevska, I. Vaskivskyi, T. Mertelj, P. Kusar, D. Svetin, S. Brazovskii, and D. Mihailovic, Ultrafast switching to a stable hidden quantum state in an electronic crystal, Science **344**, 177 (2014).

[59] Y. A. Gerasimenko, I. Vaskivskyi, M. Litskevich, J. Ravnik, J. Vodeb, M. Diego, V. Kabanov, and D. Mihailovic, Quantum jamming transition to a correlated electron glass in 1T-TaS$_2$, Nat. Mater. **18**, 1078 (2019).

[60] A. Kogar, A. Zong, P. E. Dolgirev, X. Shen, J. Straquadine, Y.-Q. Bie, X. Wang, T. Rohwer, I.-C. Tung, Y. Yang, R. Li *et al.*, Light-induced charge density wave in LaTe$_3$, Nat. Phys. **16**, 159 (2020).

[61] C. W. Nicholson, C. Berthod, M. Puppin, H. Berger, M. Wolf, M. Hoesch, and C. Monney, Dimensional crossover in a charge density wave material probed by angle-resolved photoemission spectroscopy, Phys. Rev. Lett. **118**, 206401 (2017).

[62] S. Duan, Y. Cheng, W. Xia, Y. Yang, C. Xu, F. Qi, C. Huang, T. Tang, Y. Guo, W. Luo, D. Qian, D. Xiang, J. Zhang, and W. Zhang, Optical manipulation of electronic dimensionality in a quantum material, Nature (London) **595**, 239 (2021).

[63] J. Maklar, J. Sarkar, S. Dong, Y. A. Gerasimenko, T. Pincelli, S. Beaulieu, P. S. Kirchmann, J. A. Sobota, S. Yang, D. Leuenberger *et al.*, Coherent light control of a metastable hidden state, Sci. Adv. **9**, eadi4661 (2023).

[64] A. Nakamura, T. Shimojima, Y. Chiashi, M. Kamitani, H. Sakai, S. Ishiwata, H. Li, and K. Ishizaka, Nanoscale imaging of unusual photoacoustic waves in thin flake VTe$_2$, Nano Lett. **20**, 4932 (2020).

[65] K. M. Siddiqui, D. B. Durham, F. Cropp, C. Ophus, S. Rajpurohit, Y. Zhu, J. D. Carlström, C. Stavrakas, Z. Mao, A. Raja *et al.*, Ultrafast optical melting of trimer superstructure in layered 1T'-TaTe$_2$, Commun. Phys. **4**, 152 (2021).

[66] T. C. Hu, Q. Wu, Z. X. Wang, L. Y. Shi, Q. M. Liu, L. Yue, S. J. Zhang, R. S. Li, X. Y. Zhou, S. X. Xu, D. Wu, T. Dong, and N. L. Wang, Optical spectroscopy and ultrafast pump-probe study of the structural phase transition in 1T'-TaTe$_2$, Phys. Rev. B **105**, 075113 (2022).

[67] M. Tuniz, D. Soranzio, D. Bidoggia, D. Puntel, W. Bronsch, S. L. Johnson, M. Peressi, F. Parmigiani, and F. Cilento, Ultrafast all-optical manipulation of the charge-density wave in VTe$_2$, Phys. Rev. Res. **5**, 043276 (2023).

[68] T. Suzuki, Y. Kubota, N. Mitsuishi, S. Akatsuka, J. Koga, M. Sakano, S. Masubuchi, Y. Tanaka, T. Togashi, H. Ohsumi, K. Tamasaku, M. Yabashi, H. Takahashi, S. Ishiwata, T. Machida, I. Matsuda, K. Ishizaka, and K. Okazaki, Ultrafast control of the crystal structure in a topological charge-density-wave material, Phys. Rev. B **108**, 184305 (2023).

[69] E. Canadell, S. Jobic, R. Brec, J. Rouxel, and M.-H. Whangbo, Importance of short interlayer Te···Te contacts for the structural distortions and physical properties of CdI$_2$-type layered transition-metal ditellurides, J. Solid State Chem. **99**, 189 (1992).

[70] M.-L. Doublet, S. Remy, and F. Lemoigno, Density functional theory analysis of the local chemical bonds in the periodic tantalum dichalcogenides TaX$_2$ (X=S, Se, Te), J. Chem. Phys. **113**, 5879 (2000).

[71] K. D. Bronsema, G. W. Bus, and G. A. Wiegers, The crystal structure of vanadium ditelluride, V$_{1+x}$Te$_2$, J. Solid State Chem. **53**, 415 (1984).

[72] T. Sörgel, J. Nuss, U. Wedig, R. K. Kremer, and M. Jansen, A new low temperature modification of TaTe$_2$—Comparison to the room temperature and the hypothetical 1T-TaTe$_2$ modification, Mater. Res. Bull. **41**, 987 (2006).

[73] N. Katayama, Y. Matsuda, K. Kojima, T. Hara, S. Kitou, N. Mitsuishi, H. Takahashi, S. Ishiwata, K. Ishizaka, and H. Sawa, Observation of local atomic displacements intrinsic to the double zigzag chain structure of 1T-MTe$_2$ (M = V, Nb, Ta), Phys. Rev. B **107**, 245113 (2023).

[74] J. J. Gao, J. G. Si, X. Luo, J. Yan, F. C. Chen, G. T. Lin, L. Hu, R. R. Zhang, P. Tong, W. H. Song, X. B. Zhu, W. J. Lu, and Y. P. Sun, Origin of the structural phase transition in single-crystal TaTe$_2$, Phys. Rev. B **98**, 224104 (2018).

[75] V. Petkov, K. Chapagain, J. Yang, S. Shastri, and Y. Ren, Exotic bonding interactions and coexistence of chemically distinct periodic lattice distortions in the charge density wave compound TaTe$_2$, Phys. Rev. B **102**, 024111 (2020).

[76] I. El Baggari, N. Sivadas, G. M. Stiehl, J. Waelder, D. C. Ralph, C. J. Fennie, and L. F. Kourkoutis, Direct visualization of trimerized states in 1T'-TaTe$_2$, Phys. Rev. Lett. **125**, 165302 (2020).

[77] C. Chen, H.-S. Kim, A. S. Admasu, S.-W. Cheong, K. Haule, D. Vanderbilt, and W. Wu, Trimer bonding states on the surface of the transition-metal dichalcogenide 1T'-TaTe$_2$, Phys. Rev. B **98**, 195423 (2018).

[78] I. Kar, K. Dolui, L. Harnagea, Y. Kushnirenko, G. Shipunov, N. C. Plumb, M. Shi, B. Büchner, and S. Thirupathaiah, Experimental evidence of a stable 2H phase on the surface of layered 1T'-TaTe$_2$, J. Phys. Chem. C **125**, 1150 (2021).

[79] J. Hwang, Y. Jin, C. Zhang, T. Zhu, K. Kim, Y. Zhong, J.-E. Lee, Z. Shen, Y. Chen, W. Ruan, H. Ryu, C. Hwang, J. Lee, M. F. Crommie, S.-K. Mo, and Z.-X. Shen, A novel $\sqrt{19} \times \sqrt{19}$ superstructure in epitaxially grown 1T-TaTe$_2$, Adv. Mater. **34**, 2204579 (2022).

[80] I. Di Bernardo, J. Ripoll-Sau, J. A. Silva-Guillén, F. Calleja, C. G. Ayani, R. Miranda, E. Canadell, M. Garnica, and A. L. Vázquez de Parga, Metastable polymorphic phases in monolayer TaTe$_2$, Small **19**, 2300262 (2023).

[81] W. Wang, K. Zhang, Y. Liu, A. Li, J. Li, and C. Si, Polymorphic charge density waves, magnetism, and topologies in 1T-TaTe$_2$, Phys. Rev. B **109**, 104107 (2024).

[82] H. Chen, Z. Li, L. Guo, and X. Chen, Anisotropic magnetotransport and magnetic properties of low-temperature phase of TaTe$_2$, Europhys. Lett. **117**, 27009 (2017).

[83] Y.-C. Luo, Y.-Y. Lv, R.-M. Zhang, L. Xu, Z.-A. Zhu, S.-H. Yao, J. Zhou, X.-X. Xi, Y. B. Chen, and Y.-F. Chen, Subtle effect of doping on the charge density wave in TaTe$_2$-δ ($\delta = 0.028 - 0.123$) crystals revealed by anisotropic transport measurements and Raman spectroscopy, Phys. Rev. B **103**, 064103 (2021).

[84] Y. Lin, M. Huber, S. Rajpurohit, Y. Zhu, K. M. Siddiqui, D. H. Eilbott, L. Moreschini, P. Ai, J. D. Denlinger, Z. Mao, L. Z. Tan, and A. Lanzara, Evidence of nested quasi-one-dimensional Fermi surface and decoupled charge-lattice orders in layered TaTe$_2$, Phys. Rev. Res. **4**, L022009 (2022).

[85] N. Mitsuishi, Y. Sugita, T. Akiba, Y. Takahashi, M. Sakano, K. Horiba, H. Kumigashira, H. Takahashi, S. Ishiwata, Y. Motome, and K. Ishizaka, Unveiling the orbital-selective electronic band reconstruction through the structural phase transition in TaTe$_2$, Phys. Rev. Res. **6**, 013155 (2024).

[86] A. W. Overhauser, Observability of charge-density waves by neutron diffraction, Phys. Rev. B **3**, 3173 (1971).

[87] A. Feist, N. Bach, N. Rubiano da Silva, T. Danz, M. Möller, K. E. Priebe, T. Domröse, J. G. Gatzmann, S. Rost, J. Schauss *et al.*, Ultrafast transmission electron microscopy using a laser-driven field emitter: Femtosecond resolution with a high coherence electron beam, Ultramicroscopy **176**, 63 (2017).

[88] D. Kazenwadel, N. Neathery, S. Prakash, A. Ariando, and P. Baum, Cooling times in femtosecond pump-probe experiments of phase transitions with latent heat, Phys. Rev. Res. **5**, 043077 (2023).

[89] D. H. Torchinsky, G. F. Chen, J. L. Luo, N. L. Wang, and N. Gedik, Band-dependent quasiparticle dynamics in single crystals of the Ba$_{0.6}$K$_{0.4}$Fe$_2$As$_2$ superconductor revealed by pump-probe spectroscopy, Phys. Rev. Lett. **105**, 027005 (2010).

[90] R. Y. Chen, B. F. Hu, T. Dong, and N. L. Wang, Revealing multiple charge-density-wave orders in TbTe$_3$ by optical conductivity and ultrafast pump-probe experiments, Phys. Rev. B **89**, 075114 (2014).

[91] B. Barwick, D. J. Flannigan, and A. H. Zewail, Photon-induced near-field electron microscopy, Nature (London) **462**, 902 (2009).

[92] A. Feist, K. E. Echternkamp, J. Schauss, S. V. Yalunin, S. Schäfer, and C. Ropers, Quantum coherent optical phase modulation in an ultrafast transmission electron microscope, Nature (London) **521**, 200 (2015).

[93] R. Dahan, A. Gorlach, U. Haeusler, A. Karnieli, O. Eyal, P. Yousefi, M. Segev, A. Arie, G. Eisenstein, P. Hommelhoff, and I. Kaminer, Imprinting the quantum statistics of photons on free electrons, Science **373**, eabj7128 (2021).

[94] D. A. Plemmons, S. Tae Park, A. H. Zewail, and D. J. Flannigan, Characterization of fast photoelectron packets in weak and strong laser fields in ultrafast electron microscopy, Ultramicroscopy **146**, 97 (2014).

[95] S. Hellmann, T. Rohwer, M. Kalläne, K. Hanff, C. Sohrt, A. Stange, A. Carr, M. M. Murnane, H. C. Kapteyn, L. Kipp, M. Bauer, and K. Rossnagel, Time-domain classification of charge-density-wave insulators, Nat. Commun. **3**, 1069 (2012).

[96] H. J. Zeiger, J. Vidal, T. K. Cheng, E. P. Ippen, G. Dresselhaus, and M. S. Dresselhaus, Theory for displacive excitation of coherent phonons, Phys. Rev. B **45**, 768 (1992).

[97] R. Merlin, Generating coherent THz phonons with light pulses, Solid State Commun. **102**, 207 (1997).

[98] R. Yusupov, T. Mertelj, V. V. Kabanov, S. Brazovskii, P. Kusar, J.-H. Chu, I. R. Fisher, and D. Mihailovic, Coherent dynamics of macroscopic electronic order through a symmetry breaking transition, Nat. Phys. **6**, 681 (2010).

[99] A. Zong, P. E. Dolgirev, A. Kogar, E. Ergeçen, M. B. Yilmaz, Y.-Q. Bie, T. Rohwer, I.-C. Tung, J. Straquadine, X. Wang, Y. Yang, X. Shen, R. Li, J. Yang, S. Park, M. C. Hoffmann, B. K. Ofori-Okai, M. E. Kozina, H. Wen, X. Wang *et al.*, Dynamical slowing-down in an ultrafast photoinduced phase transition, Phys. Rev. Lett. **123**, 097601 (2019).

[100] M. Huber, Y. Lin, G. Marini, L. Moreschini, C. Jozwiak, A. Bostwick, M. Calandra, and A. Lanzara, Ultrafast creation of a light-induced semimetallic state in strongly excited 1T-TiSe$_2$, Sci. Adv. **10**, eadl4481 (2024).

[101] H. Böckmann, J. G. Horstmann, A. S. Razzaq, S. Wippermann, and C. Ropers, Mode-selective ballistic pathway to a metastable electronic phase, Struct. Dyn. **9**, 045102 (2022).

[102] D. C. Miller, S. D. Mahanti, and P. M. Duxbury, Charge density wave states in tantalum dichalcogenides, Phys. Rev. B **97**, 045133 (2018).

[103] P. E. Dolgirev, A. V. Rozhkov, A. Zong, A. Kogar, N. Gedik, and B. V. Fine, Amplitude dynamics of the charge density wave in LaTe$_3$: Theoretical description of pump-probe experiments, Phys. Rev. B **101**, 054203 (2020).

[104] S. S. Philip, D. Louca, M. B. Stone, and A. I. Kolesnikov, Suppression of stacking order with doping in 1T-TaS$_{2-x}$Se$_x$, Condens. Matter **8**, 89 (2023).

[105] L.-L. Wei, S.-S. Sun, K. Sun, Y. Liu, D.-F. Shao, W.-J. Lu, Y.-P. Sun, H.-F. Tian, and H.-X. Yang, Charge density wave states and structural transition in layered chalcogenide TaSe$_{2-x}$Te$_x$, Chin. Phys. Lett. **34**, 086101 (2017).

[106] H. Luo, W. Xie, J. Tao, H. Inoue, A. Gyenis, J. W. Krizan, A. Yazdani, Y. Zhu, and R. J. Cava, Polytypism, polymorphism, and superconductivity in TaSe$_{2-x}$Te$_x$, Proc. Natl. Acad. Sci. USA **112**, E1174 (2015).

[107] J. Li, J. Li, K. Sun, L. Wu, R. Li, J. Yang, X. Shen, X. Wang, H. Luo, R. J. Cava, I. K. Robinson, X. Jin, W. Yin, Y. Zhu, and J. Tao, Concurrent probing of electron-lattice dephasing induced by photoexcitation in 1T-TaSeTe using ultrafast electron diffraction, Phys. Rev. B **101**, 100304(R) (2020).

[108] A. K. Geim and I. V. Grigorieva, Van der Waals heterostructures, Nature (London) **499**, 419 (2013).

[109] A. M. Hoque, D. Khokhriakov, B. Karpiak, and S. P. Dash, Charge-spin conversion in layered semimetal $TaTe_2$ and spin injection in van der Waals heterostructures, Phys. Rev. Res. **2**, 033204 (2020).

[110] Y.-J. Kim, W.-W. Park, H.-W. Nho, and O.-H. Kwon, High-resolution correlative imaging in ultrafast electron microscopy, Adv. Phys.: X **9**, 2316710 (2024).

[111] T. Hahn, U. Shmueli, and J. W. Arthur, *International Tables for Crystallography, Volume A: Space-Group Symmetry* (Springer, New York, 2005), Vol. 1.

[112] F. Fujimoto, Dynamical theory of electron diffraction in Laue-case, I. General theory, J. Phys. Soc. Jpn. **14**, 1558 (1959).

[113] N. Bach, T. Domröse, A. Feist, T. Rittmann, S. Strauch, C. Ropers, and S. Schäfer, Coulomb interactions in high-coherence femtosecond electron pulses from tip emitters, Struct. Dyn. **6**, 014301 (2019).